PCCP

Accepted Manuscript

ROYAL SOCIETY
OF **CHEMISTRY**

www.rsc.org/pccp

Roles of Transition Metals Interchanging
with Lithium in Electrode Materials

Tomoya Kawaguchi,[1] Katsutoshi Fukuda,[2] Kazuya Tokuda,[1] Masashi Sakaida,[1] Tetsu Ichitsubo,[1]

Masatsugu Oishi,[3] Jun'ichiro Mizuki,[4] and Eiichiro Matsubara[1]

[1]*Department of Materials Science and Engineering, Kyoto University, Kyoto 606-8501, Japan*

[2]*Office of Society-Academia Collaboration for Innovation, Kyoto University, Kyoto*

611-0011, Japan

[3]*Graduate School of Engineering, Kyoto University, Kyoto 606-8501, Japan*

[4]*School of Science and Technology, Kwansei Gakuin University, Hyogo 669-1337, Japan*

Abstract

Roles of antisite transition metals interchanging with Li atoms in electrode materials of Li transition-metal complex oxides were clarified using a newly developed direct labeling method, termed powder diffraction anomalous fine structure (P-DAFS) near the Ni K-edge. We site-selectively investigated the valence states and local structures of Ni in $Li_{0.89}Ni_{1.11}O_2$, where Ni atoms occupy mainly the NiO_2 host-layer sites and partially the interlayer Li sites inbetween the host layers, during electrochemical Li insertion/extraction in a lithium-ion battery (LIB). The site-selective x-ray near edge structure evaluated via the P-DAFS method revealed that the interlayer Ni atoms exhibited much lower electrochemical activity as compared to those at the host-layer site. Furthermore, the present analyses of site-selective extended x-ray absorption fine structure obtained from the P-DAFS method indicates local structural changes around the residual Ni atoms at the interlayer space during the initial charge; it tends to gather to form

rock-salt NiO-like domains around the interlayer Ni. The presence of the NiO-like domains in the interlayer space locally diminishes the interlayer distance and would yield strain energy because of the lattice mismatch, which retards the subsequent Li insertion both thermodynamically and kinetically. Such restrictions on the Li insertion inevitably make the NiO-like domains electrochemically inactive, resulting in an appreciable irreversible capacity after the initial charge but an achievement of robust linkage of neighboring NiO_2 layers that tend to be dissociated without the Li occupation. The P-DAFS characterization of antisite transition metals interchanging with Li atoms complements the understanding of the detailed charge-compensation and degradation mechanisms in the electrode materials.

Keywords: Antisite defect (cation mixing), lithium ion battery, site-selective analysis, diffraction anomalous fine structure, positive electrode

Introduction

Understanding crystalline and electronic structures of electrode active materials is essential for further progress of lithium ion batteries (LIBs), because the structural change and the charge compensation by ions in a solid electrode-material during lithiation/delithiation predominantly determine the electrode capabilities. These are substantially affected by the interchange between transition metal and Li atoms in the structure, i.e., known as the cation-mixing problem, which is frequently observed in the positive electrode materials.[1–7] Thus, understanding the roles of constituent atoms at different crystallographic sites in a material, which has been frequently discussed on the basis of average information in structural description, is of great importance to further develop the electrode materials.

$Li_{1-x}Ni_{1+x}O_2$ ($0 < x < 1$, identified as LNO hereafter), one of the layered rock-salt-type transition-metal oxides and a typical electrode material for LIBs, exhibits considerable antisite defects as the cation mixing. In some cases, Ni atoms occupy the interlayer space (conventionally filled with Li atoms) and the host layer, which consists of edge-sharing NiO_2 octahedra (see Fig. 1(a)). Investigating and controlling Ni at the Li sites has become a matter of concern in LIBs because of a strong correlation with battery performance.[8,9] For example, 30% of the initial charge capacity is lost in the subsequent discharge of an LNO electrode in which 11% of the Li sites are occupied by Ni atoms. In contrast to such negative effects, Ni at the Li site is known to work as a so-called "pillar" of the layered structure, which prolongs the electrode life by suppressing a destructive phase transformation that accompanies the lattice deformation.[8,10] However, quantitative evaluation of these effects induced by minor antisite defects remains challenging because of analytical difficulty in examining the experimental evidence, which tends to be masked by the dominant contribution from the host-layer transition metals.

One way to extract the information about the minor antisite defects is to utilize a site-weighted nature in x-ray diffraction (XRD). The energy dependency of an XRD intensity around an absorption edge of a selected element contains the absorption information because the magnitudes of scattering and absorption are related each other through the Kramers-Kronig relation. Furthermore, the contributions of each site to the diffraction intensity are different at each diffraction. By utilizing these features of XRD, the analytical method using diffraction anomalous fine structure (DAFS)[11–15], which is one of the x-ray resonant scattering techniques, yields site-selected x-ray absorption fine structure (XAFS) spectra. To the best of our knowledge, no DAFS approach to solving the cation-mixing problem has yet been explored, presumably because the DAFS analysis itself is considerably restricted by measurement and analytical procedures. Recently, we have developed a mathematical approach to DAFS analysis and x-ray optics that enables the acquisition of the energy dependence of XRD intensity within a short time, irrespective of sample form.[16] This versatility of the newly developed DAFS method motivates us to address the cation-mixing problem in electrode materials.

In this study, we performed powder DAFS (P-DAFS) measurements of $Li_{0.89}Ni_{1.11}O_2$ electrodes as a model material exhibiting the cation mixing before and after charge/discharge. We clarify the electrochemical activities, i.e., the redox capability, of the Ni atoms at different sites and then discuss the rearrangement of Ni at the Li sites after the initial charge. Finally, we propose a mechanism for the formation of NiO-like domains as a result of the rearrangement of Ni at the Li sites and describe how these domains affect the degradation of the electrode in the family of the layered rock-salt structures.

Results and discussion

In this study, a cell containing LNO, whose composition was determined to be $[Li_{0.89}Ni_{0.11}]_{3a}[Ni]_{3b}[O_2]_{6c}$ in the space group $R\bar{3}m$ (No. 166) by Rietveld analysis (see Supplementary Information Fig. S1), was electrochemically tested by galvanostatic charge/discharge. Here, Ni atoms at the interlayer Li sites and the host-layer Ni sites, which correspond to the 3a and 3b sites, respectively, in space group $R\bar{3}m$, are hereafter abbreviated as Ni_{Li} and Ni_{Ni}, respectively (see Fig. 1a). Figure 1b shows the resultant cyclic charge/discharge curves of the cell; the curves were measured until the end of the third discharge. In the initial cycle, the charge capacity was approximately 150 mAh g^{-1}, which corresponds to 65% Li atoms in the interlayer space having been extracted from the virgin electrode. By contrast, the discharge capacity was only 105 mAh g^{-1}. This irreversible capacity of 45 mAh g^{-1} indicates that 30% of the Li extracted from the structure during the initial charge was not reinserted into the structure during the subsequent discharge process. This irreversible capacity is known to be associated with the presence of Ni_{Li}.[8] In contrast to the initial cycle, the charge and discharge capacities in the second and the third cycles were comparable (~103 mAh g^{-1}), indicating that the electrochemical reaction occurred reversibly after the initial discharge. Interestingly, the occupancy of the Ni_{Li} and the other structural parameters obtained from the XRD pattern seemed to be nearly constant after the initial cycle (see Supplementary Information Table. S1). This observation suggests that the irreversible capacity is attributable to the electronic/local structural changes of Ni_{Li} rather than to the further occupation of the Ni atoms at the vacant Li sites. To investigate the origin of the irreversibility during the initial cycle in particular, we conducted P-DAFS measurements of LNO electrodes in the as-synthesized, charged and discharged states.

X-ray absorption near edge structure (XANES) spectra for the host-layer Ni (Ni_{Ni}) and the

interlayer Ni (Ni_{Li}) in different states of charge (SOCs) (see Figs. 2a and 2b) were obtained from the DAFS spectra (see Supplementary Information Fig. S2). In the spectra of Ni_{Ni}, the absorption edge at 8.34 keV was clearly shifted to higher energy by delithiation (charge), without a significant change of the spectrum shape, which indicates the simple oxidation of Ni_{Ni}. In the discharge process, the edge shifted in the opposite direction, reflecting the reduction of Ni_{Ni}. Thus, Ni_{Ni} is "electrochemically active," which means that these Ni atoms contribute substantially to the reversible charge compensation that accompanies lithiation/delithiation. With respect to the Ni_{Li} spectra, the absorption edge of Ni_{Li} in the as-synthesized state was located at lower energy than the absorption edge of Ni_{Ni} and was similar to the absorption edge of NiO (see Fig. 2c) in terms of shape and edge energy. Ni_{Li} is in a relatively reduced state compared with Ni_{Ni}, and the valence state of Ni_{Li} is believed to be nearly Ni^{2+}. During the initial charge process, the shoulder peak on the absorption edge indicated by arrow (1) became prominent, as indicated by arrow (2), which suggests that the electronic structure changed during charging because of the extraction of the Li atoms surrounding Ni_{Li} and the expansion of the interlayer distance (see Supplementary Information Fig. S3). No shift of the absorption edge to higher energy was observed after the charge, indicating the valence state of Ni_{Li} did not change. This observation is direct evidence that Ni_{Li} hardly contributes to the charge compensation that accompanies delithiation. The valence state and the electrochemical behavior of the Ni atoms at both sites observed in this study are consistent with the results of the site-selective *ab initio* calculation of LNO,[17] where Ni_{Li} in the reduced state makes a small contribution to the density of the state around the Fermi level; the valence state of Ni_{Li} does not significantly change by lithiation/delithiation in comparison with that of Ni_{Ni}. The XANES spectrum is sensitive to the valence change which accompanies the change in the interatomic distance of the nearest neighboring atoms. Thus, the fact that the site-selective XANES

spectrum of Ni_{Li} for the as-synthesized sample resembles those of the discharged sample indicates that the initial irreversible capacity can be attributed to local structural changes other than the nearest neighbor atoms of Ni_{Li}. For quantitative discussion of the local structural changes, we analyzed the extended x-ray fine structure (EXAFS) regions of the respective Ni atoms at different sites as follows.

Fourier transforms (FTs) of EXAFS oscillations obtained from the DAFS measurements are compared in Fig. 3a for the host-layer Ni (Ni_{Ni}) and in Fig. 3b for the interlayer Ni (Ni_{Li}) atoms. Schematic figures of the coordination environments at each Ni site are shown in Supplementary Information Fig. S4. First, we consider the FT spectra of Ni_{Ni} in Fig. 3a. Two upsurges with peak-tops at ~1.4 Å and ~2.4 Å were observed in the FT magnitude. The shorter interaction (~1.4 Å) reflecting the closest coordination is assigned to Ni_{Ni}–O. For the longer interaction at ~2.4 Å, structural information related to the Ni_{Ni}–Ni_{Ni} bond is dominant because the contributions from Li and Ni_{Li} to this peak are ignorable because of their low scattering power and low occupancy, respectively. Depending on the SOC, reversible shrinking and expansion were observed in these bonds, which were also confirmed from the fitting results of the EXAFS spectra (see Table 1). Notably, the actual bond length, which is determined by fitting the EXAFS spectrum, is larger than the length indicated by the FT magnitude in Fig. 3 because of a phase shift in the EXAFS oscillation caused by the atomic potential. The change in bond length arises from the oxidation and reduction of Ni_{Ni}, where the ionic radius changes with its valence state. Compared with Ni_{Ni}, the local structure of Ni_{Li} in Fig. 3b is significantly different. In the local structure around Ni_{Li}, the Ni_{Li}–O (2.05(4) Å) and Ni_{Li}–Ni (3.01(3) Å) bond lengths are much longer than the bond lengths of Ni_{Ni}–O (1.98(1) Å) and Ni_{Ni}–Ni_{Ni} (2.903(8) Å) before the electrochemical test (see Table 1). According to Shannon,[18] the Li–O bond length (2.16 Å) is longer than any type of Ni-O bond in six-coordination. The interlayer distance of the layered

compound is dominantly determined by the Li–O distance of Li atoms at the interlayer sites rather than by the Ni-O distance of Ni_{Li}. On the other hand, the Ni_{Li}–Ni bond consists of the Ni_{Li}–Ni_{Li} and Ni_{Li}–Ni_{Ni} contributions. In the case of the as-synthesized state (before charge), the former is negligible because the coordination number of the Ni_{Li}–Ni bond, 7(2), indicates that the Ni_{Li} atoms are isolated from each other in the interlayer space. The Ni_{Li}–Ni_{Ni} length is affected by the Li–O distance because the Ni_{Li}–Ni_{Ni} bond includes a projection of the direction normal to the NiO_2 host layer. Accordingly, the longer Ni_{Li}–O and Ni_{Li}–Ni distances observed in this study are crystallographically reasonable. The long bond length of Ni_{Li}–O supports the emergence of a relatively reduced state of Ni_{Li}, as confirmed in our site-selective XANES analysis. After the initial charge, the FT magnitude of the Ni_{Li}–Ni peak increased significantly as a result of the increased Ni_{Li}–Ni_{Li} contribution and eventually became comparable to that of NiO (see Fig. 3c). Notably, the peak heights of the Ni_{Li}–O and Ni_{Li}–Ni peaks are almost identical to the peak heights of NiO, which strongly suggests the formation of NiO-like domains around Ni_{Li} after the initial charge. In addition, the absence of distinct XRD peaks associated with NiO in the charged material suggests a short-range-ordered nature of the NiO-like domains (see Supplementary Information Fig. S1). From the fitting results shown in Table 1, the coordination numbers of the second-neighboring Ni of Ni_{Li} were 10(2), which are greater than the coordination numbers of the as-synthesized state, 7(2). This result quantitatively supports the occupation of the Ni atoms at the Li sites around Ni_{Li}, i.e., aggregation of the interlayer Ni atoms. This aggregation of the interlayer Ni atoms forms small NiO-like domains because LNO and NiO are in an isomorphic relationship, where oxygen atoms compose a face-centered cubic lattice and the cations (Ni and Li) occupy all octahedral sites of the oxygen framework; the only difference between LNO and NiO is the layer-by-layer order structure of Li and Ni along the [111] direction in the cubic lattice, which is comparable to the c-axis in the hexagonal structure

of LNO. The NiO-like domains formed during the initial charge remained after the subsequent discharge, except for a slight increase in the Ni_{Li}–O bond length. Consequently, the occupation of the NiO-like domains in the interlayer space after the first charge and its effects on the Li insertion would be essential to understanding the irreversible capacity in this system.

We now discuss the evolution mechanism of the NiO-like domains as follows. As indicated by the coordination number of the second nearest-neighbor-site in Table 1, the Ni atoms in $Li_{0.89}Ni_{1.11}O_2$ randomly occupy the interlayer Li site in the layered rock-salt structure, indicating few NiO-like domain in the as-synthesized state (see Fig. 4a). The first charge definitely triggers the aggregation of the Ni_{Li} atoms as mentioned before. A possible formation process of the NiO-like domains can be formulated as $Li_{0.31}Ni_{1.11}O_2 \rightarrow 0.22NiO + 0.89Li_{0.35}NiO_2$; the present experimental fact suggests the presence of the driving force for this reaction. This driving force is relevant to the sum of the local strain energy around the isolated Ni_{Li} atoms before the initial charge, which is attributed to the difference between the ionic radius of Ni_{Li} and the interlayer space mainly determined according as the Li concentration in the interlayer space; the radius of Ni ions is always smaller than the interlayer distance. Thus, the driving force would be enlarged by the charge because of the increase of the interlayer distance. Of course, the lattice mismatch between the LNO mother phase and the formed NiO-like domains yields the strain energy, which would be the energy barrier for the formation of the NiO-like domains; however, the present experimental result indicates that the driving force is large enough to exceed this strain-energy barrier, which results in the formation reaction of the NiO-like domains in the charged state (see Fig. 4b). Another important factor governing the formation of the NiO-like domains is the diffusion coefficient of the Ni atoms in the interlayer space. The activation energy associated with Ni diffusion in the interlayer space of a similar material has been reported to be as small as ~250 meV,[19] which is comparable to the activation energy for Li

diffusion in the interlayer.[20] Additionally, the delithiation, which yields a large amount of vacancies at the Li sites and increases the interlayer distance, promotes the diffusion of the Ni_{Li} atoms. Thus, the formation of the NiO-like domains would be driven by the electrochemical extraction of the Li atoms during the initial charge.

After the NiO-like domains are formed, Li atoms are accommodated in the interlayer space, except for the exclusive space occupied by the NiO-like domains in the process of subsequent discharge. Undoubtedly, the irreversible capacity observed in the initial cycle correlates to the formation of NiO-like domains. This irreversibility is believed to depend on the discharge conditions. For instance, Li can be almost completely reinserted when the electrode is kept at a low potential of 2.0 V vs. Li^+/Li for as long as one month.[8] This example indicates that the irreversible capacity of this system may be governed by both the thermodynamic driving force and the kinetic effect associated with Li diffusion. Importantly, the formation of the NiO-like domains in the mother phase of the layered structure yields the inevitable coherent strain around this Ni_{Li} because of the lattice mismatch (see Fig. 4c). The Ni-O bond length (2.07 Å, see Table 1) is smaller than the Li-O bond length (2.1157 Å, see Table S1) in the discharged sample, which results in a 2.16% shrinkage of the interlayer space around the NiO-like domains. This strain is one of the most likely reasons for the irreversible capacity in the initial cycle. The chemical potential of Li increases because of the elastic-strain energy, which means the decrease in the intercalation potential of Li around the NiO-like domains.[21–24] Consequently, facile Li insertion is thermodynamically retarded because of the decrease in the driving force for the insertion. From a kinetic perspective, a decrease in the interlayer space increases the activation energy of the Li diffusion and consequently also disturbs the facile Li insertion. These thermodynamic and kinetic factors that stem from the existence of the NiO-like domains hinder Li insertion during discharge and result in the irreversible capacity.

The issue of how the NiO-like domains function in this active material during charge/discharge cycles is also an important consideration. The results of our P-DAFS study suggest that the coordination number of Ni_{Li}-Ni reaches almost 10, being comparable to 12 for rock-salt structured NiO with no Li sites in the crystal structure after the initial charge, which indicates that the NiO-like domain of the highly dense structure would exhibit an electrochemically inactive nature. In addition, the NiO-like domains are not significantly modified during discharge with respect to the bond length or the valence. Such a concrete structure may function as a pillar to link two neighboring NiO_2 layers and restrain the structural destruction that is known to occur in $LiNiO_2$ without antisite Ni_{Li} atoms. As a result, the extensive gathering of the Ni atoms in the interlayer to form the NiO-like domain enhances the cyclability of this electrode. This result is compatible with the well-studied relationship between the amount of Ni_{Li} atoms and cyclability.[25–27]

Concluding remarks

In this study, we analyzed site-selectively the electronic and local structures of Ni atoms occupying both host-layer and interlayer sites during the initial charge/discharge cycle by the newly developed P-DAFS method. On the basis of the XANES and EXAFS analyses at each site obtained from the P-DAFS spectra, we observed that Ni_{Li} exhibited low electrochemical activity and did not undergo reversible valence changes for the charge compensation during the charge/discharge, whereas Ni_{Ni} exhibited reversible changes. The quantitative analysis of the EXAFS spectra at Ni_{Li} suggested the aggregation of randomly isolated Ni atoms occupying the Li site at the as-synthesized state, i.e., the formation of NiO-like domains, after the initial charge.

The presence of the NiO-like domains in the interlayer space yielded a considerable strain field

around the domain, which disturbed the facile Li insertion during the subsequent discharge process both energetically and kinetically. The decrease of the Li occupation due to the slow diffusion around the NiO-like domains results in the irreversible electrochemical reaction occurred during the initial cycle. In addition, the low electrochemical activity of the Ni_{Li} atoms in this system can be understood by the drastic change in the local structure of Ni_{Li}. The well-known "pillar effect" to suppress the structural destruction during charge originated in the electrochemically inactive NiO-like domains observed in this study rather than the isolated interlayer Ni atoms. These findings are highly useful for discussing the structural stability and degradation mechanism of other electrode materials, including the promising Li-rich layered transition-metal oxides, which also exhibit the considerable cation-mixing. This study demonstrates the great potential of site-distinguished analysis for electrode materials by the P-DAFS method and emphasizes the importance of understanding the roles of the constituent elements in the electrode materials on the basis of new insights into the "cation-mixing problem". The complemental understanding of the roles of antisite transition metals interchanging with Li will open a path for new material design positively utilizing the defects in LIBs.

Experimental

Sample preparation

A commercial $Li_{0.89}Ni_{1.11}O_2$ (Toshima Co., Ltd.), whose structure was refined by the Rietveld method according to the established protocol[27] using the RIETAN-FP[28] software and is denoted as $[Li_{0.89}Ni_{0.11}]_{3a}[Ni]_{3b}[O_2]_{6c}$ in space group $R\bar{3}m$ (No. 166) (see Supplementary Information Fig. S1 and Table S1), was used as an active material. A composite electrode that consisted of 88 wt% active material, 6 wt% carbon black and 6 wt% polyvinylidene difluoride was prepared

by coating the slurry onto a 25 mm × 15 mm Al metal foil. The applied electrode was dried at 80°C under vacuum overnight. The cells for the electrochemical tests were assembled with the obtained composite electrode for the positive electrode (i.e., working electrode), Li metal plates (Honjo Metal Co., Ltd.) for the reference and negative electrodes (i.e., counter electrode) and an electrolyte of 1 mol dm^{-3} LiPF$_6$ in a mixed solvent of ethylene carbonate (EC)/dimethyl carbonate (DMC) (1/2 in volume, Kishida Chemical), in an Ar-filled dry box, where the dew point was less than -80°C. The cycle tests were conducted with an HJ1001SD8 apparatus (Hokuto Denko Co., Ltd.) at a charge rate of 32 mA g^{-1} (C-rate of 0.2C assuming a theoretical capacity of 160 mAh g^{-1}, which corresponds to 0.58 Li in stoichiometric LiNiO$_2$); the cut-off voltages were set at 4.2 V and 2.5 V vs. Li$^+$/Li for charge and discharge, respectively.

Electrode samples for the P-DAFS measurements were cycled in the same manner but at a charge/discharge rate of 3.2 mAh g^{-1} (0.02C) to assure a homogeneous reaction at the electrode. The cycled cells were disassembled in an Ar-filled dry box. The electrodes were removed from the cells, washed sequentially with EC/DMC (1/2 by volume) and DMC, and then dried under vacuum in a side box of the dry box. The composite was removed from the Al collector and pelletized into a 6-mm-diameter disc with BN powder as a diluent for the P-DAFS analysis. Typical weights of the composite and BN were ~2 mg and 15 mg, respectively. Obtained pellets were packed with polyimide tape to prevent the infiltration of moist air during the P-DAFS measurements.

P-DAFS measurements and analysis

The P-DAFS measurements were conducted at beamline BL28XU,[29,30] SPring-8, Japan. We used a Si (111) channel-cut monochromator with a 3-mm gap in combination with two pairs of horizontal and vertical Rh-coated mirrors upstream and downstream of the monochromator to

eliminate high-order harmonics. The incident beam was shaped into 500-□m horizontal and 200-□m vertical widths on the sample using a quadrant slit. Two ionization chambers with He and N_2 gas flows were located upstream and downstream of the sample to monitor the absorption around the absorption edge, which was used for the absorption correction of the DAFS spectra. A two-dimensional Pilatus detector (Dectris Co., Ltd.) was mounted onto a 2θ arm of a multi-axis goniometer and was used to measure the diffraction profile. The distance from the sample to the detector was 523.2 mm, ensuring the simultaneous measurement of 9° in 2θ.

The DAFS spectra of LNO were measured from the 003 and 104 diffraction peaks between 8.007 and 9.307 keV, where the accumulation time was differently set to ensure sufficient photon statistics. We rotated the pellet sample on the axis perpendicular to the sample surface to improve the particle statistics during the measurements. The integrated intensities of the observed peaks were determined by least-squares fitting using Toraya's split pseudo-Voigt peak function[31] with a linear background.

The obtained DAFS spectra were analyzed by the logarithmic dispersion relation (LDR) method described in detail in our previous paper.[16] The spectra were corrected for the incident beam intensity, the Lorentz-polarization factor and the absorption factor, including the particle absorption factor.[32] The absorption factor was calculated from the experimental absorption coefficient from the XAFS spectra and the scattering path in the pellet sample. The magnitude of the particle absorption factor was estimated by comparing the 104 DAFS spectra and the XAFS spectra, where the contribution from each site is nearly identical; the same particle absorption factor was used to correct the 003 DAFS spectra, and spherical particles were assumed for the absorption calculation of the particle absorption factor. The truncation errors of infinite integration in the LDR analysis were corrected using the phases calculated from the

structure parameters obtained from the Rietveld refinement at each composition and the theoretically calculated resonant terms[33] at 8.320 and 9.200 keV, where the oscillation was substantially damped. The scaling factors for conversion to the electron unit were determined by comparing the experimental DAFS spectra at the lowest and highest energies with the spectra calculated from the structure parameters obtained from the Rietveld refinements. The XAFS-like spectra at each site were separated by the 003 DAFS and the XAFS spectra to obtain quality spectra based on the structural parameters.

The XAFS spectrum at each site obtained from DAFS was analyzed using the IFEFFIT program code.[34] The postedge background was removed by the Autobk algorithm using an r_{bkg} value of 0.9. The normalized XAFS-like spectra were converted from energy to wave number k, then weighted by k^2 for extended absorption fine structure (EXAFS) analyses. Fourier-transform magnitudes were evaluated from the weighted data of Ni_{Li} and Ni_{Ni} sites ranging from 1.8 Å^{-1} to 12.7 Å^{-1} and from 2 Å^{-1} to 13 Å^{-1}, respectively. The first and second coordination shells, which correspond to Ni-O and Ni-Ni bonds, respectively, were fitted in the radial space with the backscattering amplitudes and phase shifts calculated by the FEFF code; all the resultant R-factors (i.e., goodness of the fittings) were less than 0.22 and 0.07 in Ni_{Li} and Ni_{Ni}, respectively. In the fittings of Ni_{Ni}, we used modified structure models with the refined structure parameters from the Rietveld analysis, where the antisite defect was neglected for the sake of simplicity in the FEFF calculation; both the bond lengths of Ni-O and Ni-Ni were refined. In the fittings of Ni_{Li}, the model structures were constructed from a $2 \times 2 \times 1$ ($a \times b \times c$ axes) supercell of the pristine hexagonal lattice, where the interlayer Li atoms were substituted by Ni atoms. In the as-synthesized sample, one Li atom was substituted for a Ni atom to introduce the antisite defect; the FEFF calculation was performed at this Ni atom. Both in the charged and discharged samples, all Li atoms in one layer were substituted for Ni atoms, and the calculation was

performed at the inserted interlayer Ni atom. In the EXAFS analyses of the Ni_{Li} atoms using the above-mentioned models, we evaluated the coordination number of the second coordination shell of the central Ni_{Li} atom and the Ni-O and Ni-Ni bond lengths. The same amplitude reduction term of 0.97 determined from preliminary fitting of the NiO EXAFS measured in the same beam time was used in all fittings of LNO. The Debye-Waller factors of Ni (0.0052 Å) and O (0.0136 Å) refined by fitting the EXAFS of Ni_{Ni} in the as-synthesized sample were used in the subsequent fittings of the other LNO samples.

Acknowledgments

References

1.   N. Yabuuchi, K. Yoshii, S.-T. Myung, I. Nakai, and S. Komaba, *J. Am. Chem. Soc.*, 2011, **133**, 4404–4419.

2.   N. Tran, L. Croguennec, M. Me, F. Weill, P. Biensan, C. Jordy, and C. Delmas, *Chem. Mater.*, 2008, **20**, 4815–4825.

3.   A. R. Armstrong and P. G. Bruce, *Lett. To Nat.*, 1996, **381**, 499.

4.   A. R. Armstrong, A. J. Paterson, N. Dupré, C. P. Grey, and P. G. Bruce, *Chem. Mater.*, 2007, **19**, 1016–1023.

5.   S. Mishra and G. Ceder, *Phys. Rev. B*, 1999, **59**, 6120–6130.

6.   Y. Shao-Horn, S. A. Hackney, A. R. Armstrong, P. G. Bruce, R. Gitzendanner, C. S. Johnson, and M. M. Thacheray, *J. Electrochem. Soc.*, 1999, **146**, 2404–2412.

7.   J. Lee, A. Urban, X. Li, D. Su, G. Hautier, and G. Ceder, *Science*, 2014, **343**, 519–22.

8.   J. P. Peres, C. Delmas, A. Rougier, M. Broussely, F. Perton, P. Biensan, and P. Willmann, *J. Phys. Chem. Solids*, 1996, **57**, 1057–1060.

9.   J. Molenda, P. Wilk, and J. Marzec, *Solid State Ionics*, 2002, **146**, 73–79.

10.   R. V. Moshtev, P. Zlatilova, V. Manev, and A. Sato, *J. Power Sources*, 1995, **54**, 329–333.

11.   H. Stragier, J. Cross, J. Rehr, L. Sorensen, C. E. Bouldin, and J. C. Woicik, *Phys. Rev. Lett.*, 1992, **69**, 3064–3067.

12.   D. J. Tweet, K. Akimoto, I. Hirosawa, T. Tatsumi, H. Kimura, J. Mizuki, L. B. Sorensen, C. E. Bouldin, and T. Matsushita, *Jpn. J. Appl. Phys.*, 1992, **32**, 203–205.

13.   I. J. Pickering, M. Sansone, J. Mars, and G. N. George, *J. Am. Chem. Soc.*, 1993, **115**, 6302–6311.

14.   M. Zschornak, C. Richter, M. Nentwich, H. Stöcker, S. Gemming, and D. C. Meyer, *Cryst. Res. Technol.*, 2014, **49**, 43–54.

15.   V. Favre-Nicolin, M. G. Proietti, C. Leclere, N. A. Katcho, M.-I. Richard, and H. Renevier, *Eur. Phys. J. Spec. Top.*, 2012, **208**, 189–216.

16.   T. Kawaguchi, K. Fukuda, K. Tokuda, K. Shimada, T. Ichitsubo, M. Oishi, J. Mizuki, and E. Matsubara, *J. Synchrotron Radiat.*, 2014, **21**, 1247–1251.

17.   Y. Koyama, H. Arai, I. Tanaka, Y. Uchimoto, and Z. Ogumi, *Chem. Mater.*, 2012, **24**, 3886–3894.

18.   R. D. Shannon, *Acta Cryst.*, 1976, **A32**, 751–767.

19.   M. Gu, I. Belharouak, A. Genc, Z. Wang, D. Wang, K. Amine, F. Gao, G. Zhou, S. Thevuthasan, D. R. Baer, J.-G. Zhang, N. D. Browning, J. Liu, and C. Wang, *Nano Lett.*, 2012, **12**, 5186–5191.

20.   A. Van Der Ven and G. Ceder, *Electrochem. Solid-State Lett.*, 2000, **3**, 301–304.

21.   T. Ichitsubo, K. Tokuda, S. Yagi, M. Kawamori, T. Kawaguchi, T. Doi, M. Oishi, and E. Matsubara, *J. Mater. Chem. A*, 2013, **1**, 2567–2577.

22.   T. Ichitsubo, S. Yukitani, K. Hirai, S. Yagi, T. Uda, and E. Matsubara, *J. Mater. Chem.*, 2011, **21**, 2701–2708.

23.   K. Hirai, T. Ichitsubo, T. Uda, A. Miyazaki, S. Yagi, and E. Matsubara, *Acta Mater.*, 2008, **56**, 1539–1545.

24.   D. A. Cogswell and M. Z. Bazant, *ACS Nano*, 2012, **6**, 2215–2225.

25.   A. Hirano, R. Kanno, Y. Kawamoto, Y. Takeda, K. Yamaura, M. Takano, K. Ohyama, M. Ohashi, and Y. Yamaguchi, *Solid State Ionics*, 1995, **78**, 123–131.

26.   A. Hirano, R. Kanno, Y. Kawamoto, K. Oikawa, T. Kamiyama, and F. Izumi, *Solid State Ionics*, 1996, **86–88**, 791–796.

27.   H. Arai, S. Okada, H. Ohtsuka, M. Ichimura, and J. Yamaki, *Solid State Ionics*, 1995, **80**, 261–269.

28.   F. Izumi and K. Momma, *Solid State Phenom.*, 2007, **130**, 15–20.

29.   H. Tanida, K. Fukuda, H. Murayama, Y. Orikasa, H. Arai, Y. Uchimoto, E. Matsubara, T. Uruga, K. Takeshita, S. Takahashi, M. Sano, H. Aoyagi, A. Watanabe, N. Nariyama, H. Ohashi, H. Yumoto, T. Koyama, Y. Senba, T. Takeuchi, Y. Furukawa, T. Ohata, T. Matsushita, Y. Ishizawa, T. Kudo, H. Kimura, H. Yamazaki, T. Tanaka, T. Bizen, T. Seike, S. Goto, H. Ohno, M. Takata, H. Kitamura, T. Ishikawa, T. Ohta, and Z. Ogumi, *J. Synchrotron Radiat.*, 2014, **21**, 268–272.

30.   K. Tokuda, T. Kawaguchi, K. Fukuda, T. Ichitsubo, and E. Matsubara, *APL Mater.*, 2014, **2**, 070701.

31.   H. Toraya, *J. Appl. Crystallogr.*, 1990, **23**, 485–491.

32. G. W. Brindley, *Philos. Mag. Ser. 7*, 1945, **36**, 347–369.

33. S. Sasaki, *KEK Rep.*, 1989, **88-14**, 1.

34. B. Ravel and M. Newville, *J. Synchrotron Radiat.*, 2005, **12**, 537–541.

35. K. Momma and F. Izumi, *J. Appl. Crystallogr.*, 2011, **44**, 1272–1276.

36. J. J. Rehr, J. J. Kas, F. D. Vila, M. P. Prange, and K. Jorissen, *Phys. Chem. Chem. Phys.*,
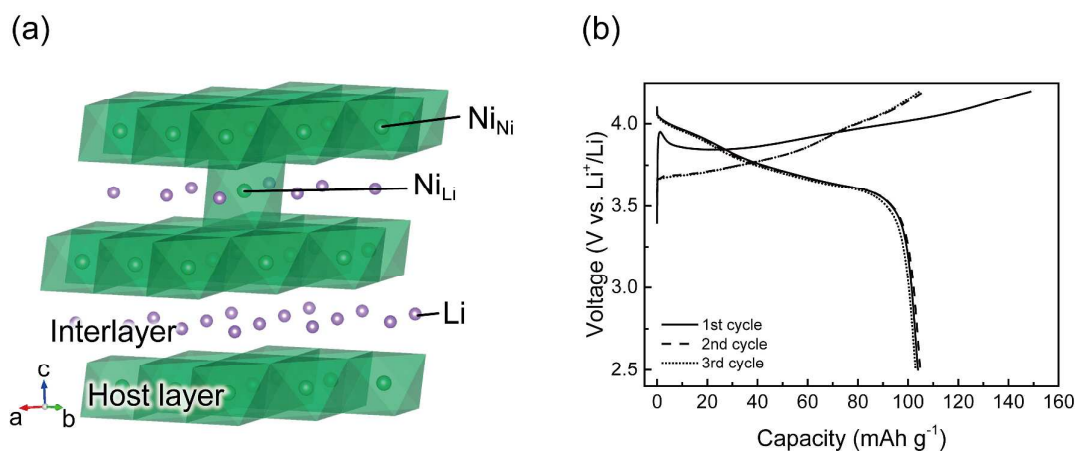2010, **12**, 5503–5513.

Figures and captions

(a)

(b)

Figure 1. (a) Structure of $Li_{1-x}Ni_{1+x}O_2$. The green polyhedra represent the NiO_6 octahedra. (b)

Charge/discharge curves of $Li_{0.89}Ni_{1.11}O_2$ in the (solid) 1st cycle, (broken) 2nd cycle and (dotted)
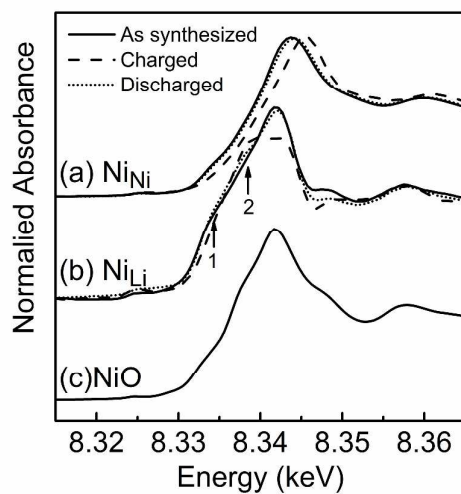
3rd cycle.

Figure 2. XANES spectra of Ni in LNO (a) at the host-layer Ni site (Ni_{Ni}) and (b) at the interlayer site (Ni_{Li}), both of which were obtained from DAFS, and (c) a XANES spectrum of NiO for comparison. Solid, broken and dotted lines correspond to the as-synthesized, charged and discharged states, respectively. Arrows indicate the shoulder peaks on the absorption edge of (1) as-synthesized and (2) charged states.
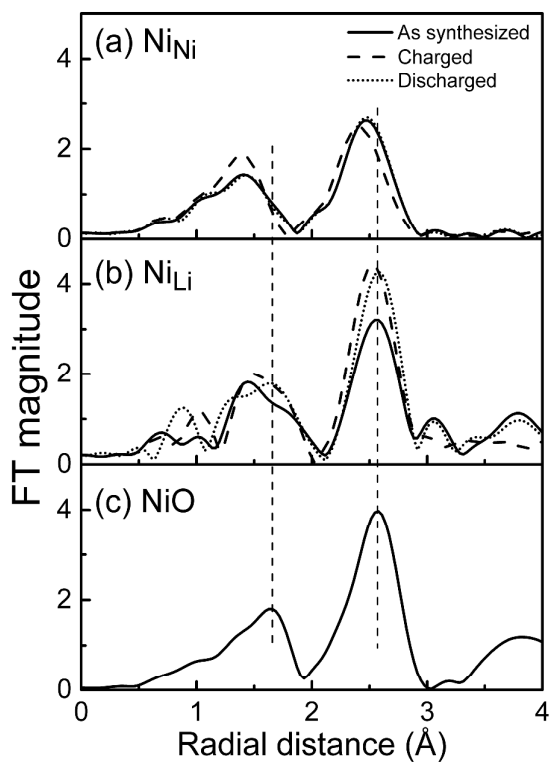
Figure 3. FT magnitude obtained from the EXAFS regions of Ni in LNO (a) at the host-layer Ni site (Ni_{Ni}) and (b) at the interlayer site (Ni_{Li}), both of which were obtained from DAFS; (c) FT magnitude of NiO obtained from the XAFS measurement for comparison. Solid, broken and dotted lines correspond to the as-synthesized, charged and discharged states, respectively.

Table 1. Comparison of the local structures around Ni atoms at different crystallographic sites.

Sample	State	Site	Ni-O bond length (Å)	Ni-Ni bond length (Å)	CN of Ni-Ni [a]
$Li_{0.89-x}Ni_{1.11}O_2$	As synthesized	Ni (3b)	1.98(1) [b]	2.903(8)	6
	Charged	Ni (3b)	1.92(2)	2.86(1)	6
	Discharged	Ni (3b)	1.98(1)	2.901(7)	6
	As synthesized	Li (3a)	2.05(4)	3.01(3)	7(2)
	Charged	Li (3a)	2.04(4)	2.98(2)	10(2)
	Discharged	Li (3a)	2.07(4)	3.02(2)	10(2)
cf. NiO		Ni	2.093(3)	2.960(4)	12

[a] CN of Ni-Ni: coordination number of the second coordination shell around Ni atoms.

[b] The number in the bracket indicates the standard deviation estimated using the nonlinear

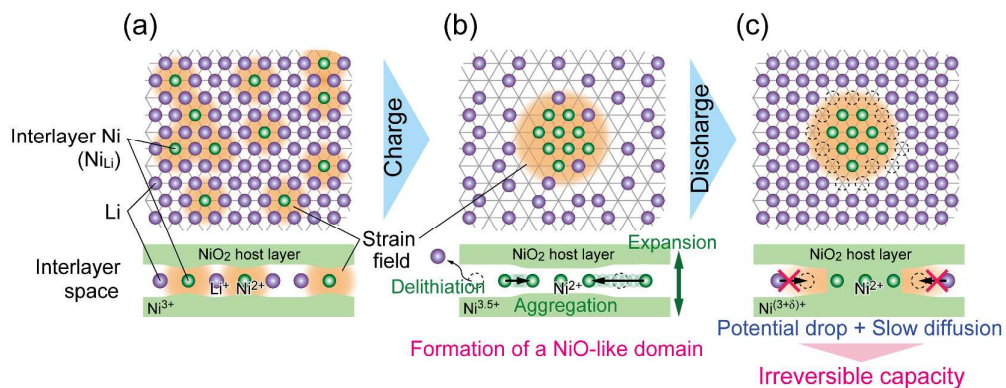least-squares method on the last digit, e.g., $1.98(1)$ means 1.98 ± 0.01.

Figure 4. Schematic model for the formation of NiO-like domains during charging. (a) Li and Ni distribution in the interlayer space along the *c*-axis (upper) and *a*-axis (lower). (b) Aggregation of Ni after the initial charge. (c) Interlayer space after the discharge.